Journal of The
Electrochemical Society

The Electrochemical Society

Impact of Module Configuration on Lithium-Ion Battery Performance and Degradation: Part I. Energy Throughput, Voltage Spread, and Current Distribution

To cite this article: Yuliya Preger *et al* 2025 *J. Electrochem. Soc.* **172** 050540

Journal of The Electrochemical Society, 2025 **172** 050540

Impact of Module Configuration on Lithium-Ion Battery Performance and Degradation: Part I. Energy Throughput, Voltage Spread, and Current Distribution

Yuliya Preger,[1,=,*,z] Jacob Mueller,[2,=,z] Armando Fresquez,[3] Srikanth Allu,[4,*] and Chaz Rich[5]

[1]*Energy Storage Technology and Systems, Sandia National Laboratories, Albuquerque, New Mexico, United States of America*
[2]*Power Electronic and Energy Conversion Systems, Sandia National Laboratories, Albuquerque, New Mexico, United States of America*
[3]*Enterprise Assurance and Risk Management, Sandia National Laboratories, Albuquerque, New Mexico, United States of America*
[4]*Computational Sciences and Engineering Division, Oak Ridge National Lab, Oak Ridge, Tennessee, United States of America*
[5]*Power Sources R&D, Sandia National Laboratories, Albuquerque, New Mexico, United States of America*

Batteries are commonly connected in series and parallel to create modules that fulfill the power and energy requirements of specific applications. However, conclusions about battery performance and degradation under different conditions, as well as predictive models, are often derived from single cell cycling results. In this study, we evaluate the performance of six different series-parallel configurations of commercial lithium nickel manganese cobalt cells over hundreds of cycles. Each cell within the modules was individually instrumented for voltage, current, and temperature monitoring. We quantified the impact of module configuration on overall energy throughput, the voltage spread among series-connected cells, and the current heterogeneity in parallel-connected cells. This module cycling study, one of the broadest reported to date, supports systematic evaluation of the performance trade-offs, pack penalty, and safety implications of different module configurations.
 [DOI: 10.1149/1945-7111/add777]

Manuscript submitted January 16, 2025; revised manuscript received March 31, 2025. Published May 29, 2025.

Supplementary material for this article is available online

Lithium-ion (Li-ion) batteries are deployed in a wide range of applications including consumer electronics, electric vehicles, and stationary energy storage systems. Expectations about battery performance and degradation in these applications are often derived by scaling single cell cycling results. Single cell results can be valuable for objectives such as understanding the general impact of different cycling conditions on degradation[1–5] or identifying cells with suitable properties for different applications and duty profiles.[6–9] However, dozens of cells are typically connected in series and parallel to form modules that meet the power and energy requirements of larger-scale applications. A series connection is considered for overall voltage scaling whereas a parallel connection is employed for current scaling that leads to increased capacity and energy storage of the module configuration. Cells in modules can encounter new electrical and thermal phenomena that prevent direct scaling of single cell experimental results (colloquially called the "pack penalty"). Electrical imbalances primarily arise from variations in cell capacities, internal and external impedances, or aging rates, which can lead to uneven charge and discharge. Cell imbalance is particularly detrimental in series configurations, as all cells must carry the same current; weaker cells limit the net capacity, resulting in sub-optimal performance. Additionally, poor thermal management of the cells in modules can lead to non-uniform heating, accelerating cell degradation and reducing the overall lifespan of the system. Evaluating module-level performance experimentally is particularly challenging due to the increased fabrication and electrical facility requirements, but it is critical for designing better energy storage systems and accurately predicting their performance.

Previous studies of module cycling have explored different phenomena that arise when cells are connected. Many computational studies, primarily based on equivalent circuit models, have shown how cell-to-cell variation can diminish the overall module capacity and lifetime.[10–20] Other studies have demonstrated how variations in cell resistance and capacity, as well as interconnect resistance, can impact current distribution in parallel strings.[21–35] Several authors have also examined how thermal variation across a battery module can lead to different cell aging rates and an overall higher degradation rate for the module.[30,36–44] While these studies have shed light on important phenomena, they are generally limited in the breadth of experimental data available to validate the resulting models. Many have exclusively studied 2P-1S or 3P-1S configurations. When more complex or larger modules are studied, there is often limited long-term cycling data to show how behaviors change over time.[40,45–54] Furthermore, few studies collect cell-level data that would lend greater insight into the causes of module-level performance degradation.

In this study, we assess the performance of twelve modules of NMC ($LiNi_xMn_yCo_{1-x-y}O_2$) cells in six different configurations (8P-1S, 4P-2S, 2P-4S, 2S-4P, 4S-2P, and 8S-1P) over the course of four hundred cycles. Voltage, current, and temperature data were collected for each cell in each module. We quantified the impact of module configuration on overall energy throughput, the voltage-spread in series-connected cells, and the current heterogeneity in parallel-connected cells. A future publication will further describe the impact of parallelization on module performance, including cell energy throughput and degradation, and the role of cell position and temperature heterogeneity. This module cycling study enables systematic evaluation of the performance trade-offs and safety implications of different module configurations. Cycling data will be made available at www.batteryarchive.org to facilitate future experimental and modeling efforts.

Experimental Methods

Cell specifications.—The modules were populated with commercial 18650 NMC cells from LG Chem (Part #18650HG2, 3 Ah).

[=]Equal Contribution.
*Electrochemical Society Member.
[z]E-mail: ypreger@sandia.gov; jmuelle@sandia.gov

According to previous ICP characterization, the cathode is NMC811 and the anode is graphite with some silicon.[55] We followed the manufacturer-recommended operating conditions for this cell (listed in Table S1).

Module design.—The study used six different module configurations (8P-1S, 4P-2S, 2P-4S, 2S-4P, 4S-2P, and 8S-1P). Modules were constructed from a common printed circuit board (PCB). The PCB was designed around several objectives:

- Support all six module configurations.
- Standardize cell spacing and arrangement across module configurations.
- Facilitate in-circuit cell-level voltage and current sensing.
- Enable nondestructive cell removal/reinsertion for individual cell state-of-health measurements.
- Where possible, leverage conductive materials typical of real-world battery packs to accurately emulate practical cell interconnection resistances.

Cells attach to the circuit board through cylindrical cell-to-board battery contact clips which are soldered to the PCB (Fig. 1). These clips use spring tension to maintain electrical connection with the electrodes. This enables repeatable cell extraction and insertion, which would not be possible with direct welds or soldered electrode connections. However, the amount of tension applied by the clip varies greatly, leading to inconsistent contact resistance. The module design addresses this through a 3D-printed mechanical assembly. The assembly applies a controllable amount of force to the back side of the battery clips, ensuring consistent contact. An adjustable torque driver was used to set the amount of force applied to the clip at either electrode. Thumb nuts on either side of the cell lock the assembly into position. To validate this approach for ensuring consistent contact resistance, we used a nickel cylinder with the same shape as an 18650 cell and known end-to-end resistance. Using this blank, we were able to verify that the total resistance across the blank-and-clip connections was constant through multiple insertions and removals.

Module configurations were implemented from the common PCB by selectively populating cell-to-cell or cell-to-busbar interconnections with nickel ribbon. The PCB itself only conducts charging/discharging current between the conductive cell holders and solder pads, which serve as the point of attachment for nickel ribbons. For each cell, two solder pads are provided per electrode. One set of solder pads is used to form series connections of cells. A nickel ribbon is placed between the negative electrode pad of one cell and the positive electrode pad of its adjacent cell. The second set of solder pads is used to facilitate busbar connections, thereby forming parallel cell connections. All soldered nickel ribbon connections use leaded solder and Kester 2331ZX flux. Laser welds were used to connect nickel ribbons to busbars. The specific cell-to-cell and cell-to-busbar interconnections for each module are shown in Fig. S1.

The PCBs were designed to minimize the introduction of interconnect resistances that would interfere with the measurement of battery phenomena. Four-point resistance measurements of the cell-to-cell and cell-to-busbar interconnections were taken using an Agilent 3458a multimeter with a resolution of 10 $\mu\Omega$. The cell-to-cell interconnections (Ni tab at the negative electrode pad of one cell to the positive electrode pad of the adjacent cell) were 4.4 +/− 0.2 mΩ across all modules. The cell-to-busbar interconnections were 2.5 +/− 0.3 mΩ on the negative side (from the Ni tab at the negative electrode terminal to the busbar on the negative terminal side) and 4.8 +/− 0.4 mΩ on the positive side (from the Ni tab at the positive electrode terminal to the busbar on the positive terminal side), with the higher resistance on the positive side attributed to the longer conduction path and the Hall-effect current sensors.

To enable cell-level current sensing, a LEM LTS-15NP current sensor was placed between each cell's positive electrode and busbar connection solder pad. In this configuration, any parallel cell (or branch of cells) flows through a dedicated sensor. The LTS-15NP is a closed-loop Hall effect sensor, which provides high sensing accuracy with less than 1 mΩ of insertion resistance. This low series resistance ensures that current sharing behaviors are not artificially influenced by the sensor. The output of the sensors is unipolar, centered at 2.5 V, with sensitivity of 41.6 mV A^{-1}. Analog signal conditioning circuits map this output voltage to the ±5 V range of the auxiliary input channels of the module cycler. This simple signal conditioning circuit removes the 2.5 V offset and applies a gain of 10, producing a cell-level current sensing range of ±12.5 A. Raw board power was provided to the PCBs by a Teledyne T3PS43203 32 V/3 A power supply. Isolated DC-DC converters integrated onto the PCBs condition the input power, providing electronics with precisely regulated source voltages and reducing susceptibility to conducted noise from the supply. The Supporting Information details the calibration procedure for data from these current sensors.

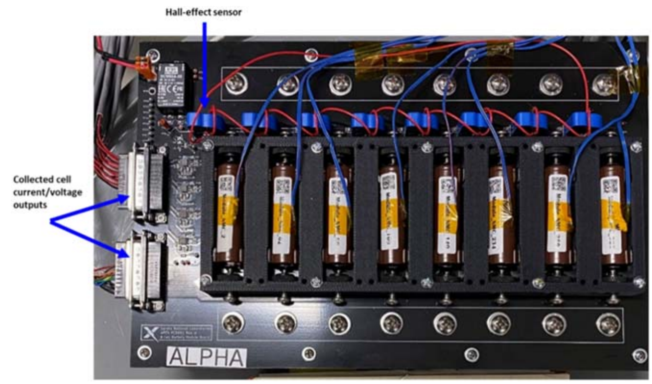

Figure 1. Photo of 8P-1S module board.

The PCB also enabled cell-level voltage measurements by providing a direct connection from each cell electrode to the auxiliary channels of the module tester. No signal conditioning was necessary for cell voltage measurements. Cell voltages and current sensor output signals collect at D-SUB cable ports to simplify signal connection to the module tester.

Overall study approach.—We completed initial characterization (mass and capacity check) of a lot of 400 cells. Two sets of well-matched cells (96 in total) were selected for module testing. Each module was populated with the first set of cells and completed two hundred cycles at so-called "mild conditions" and two hundred cycles at more "aggressive conditions" (wider voltage window and higher discharge rate). The first set of cells was then removed from each module and all cells underwent a final capacity check. This testing routine was then repeated with the second set of cells to check the consistency of the results.

Cell characterization.—This study involved six different module configurations of eight cells each (48 cells) and two sets of experiments, so 96 cells were required. Four hundred cells from the same lot were weighed and underwent a capacity health check to assess the initial variation in the lot.

The cell cycling was carried out using an Arbin high-precision (Model: LBT21084) multi-channel battery testing system. Individual cells were placed into commercially available 18650 battery holders from Memory Protection Devices. The holders were connected to the Arbin with 18-gauge wire and the cable lengths kept below eight feet to minimize voltage drop. The cells were placed in a SPX Tenney Model T10C-1.5 environmental chamber, which can be controlled between −73 °C and 200 °C. A K- or T-type thermocouple was attached to the skin of each cell under test with Kapton tape to monitor the cell skin temperature. During characterization, the chamber was kept at 25 °C and the as-received cells were kept in

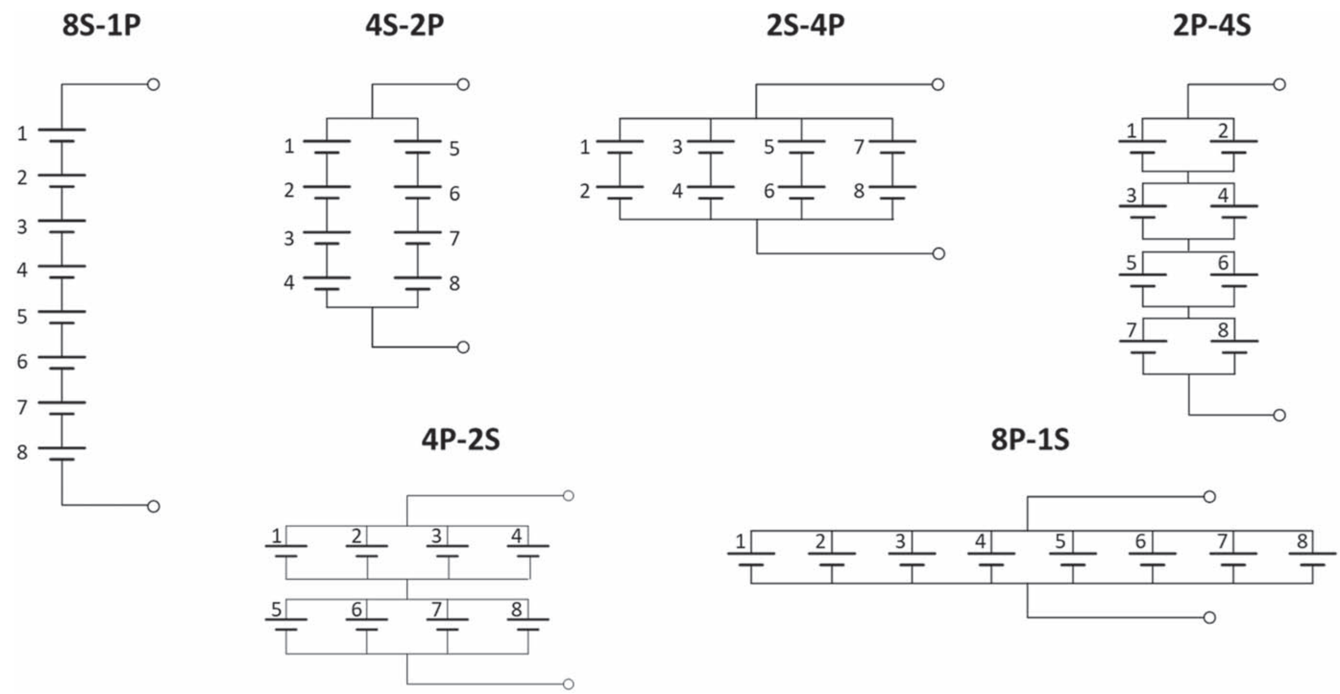

Figure 2. Module configurations considered in this study. The numbers 1–8 indicate the cell positions in each module and are referenced in subsequent figures.

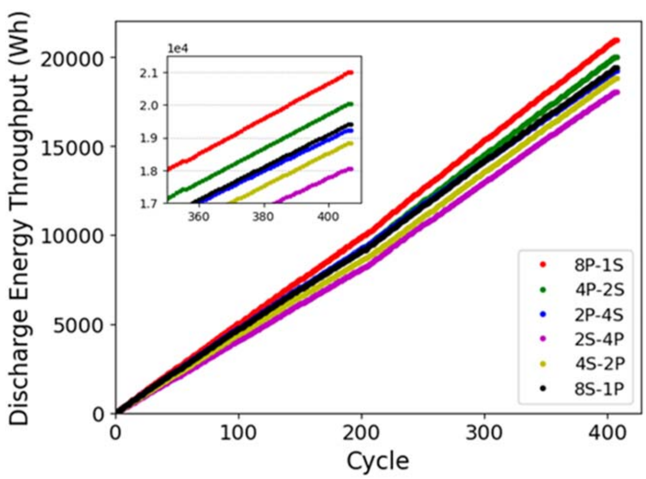

Figure 3. Cumulative discharge energy throughput for all modules in Set 1. Values are reported after each cycle. Each color indicates a different module configuration.

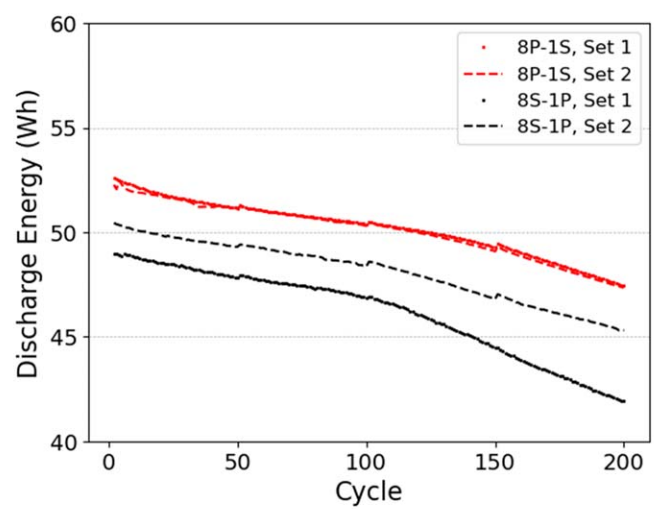

Figure 4. Discharge energy fade rate for the 8P-1S (red) and 8S-1P (black) configurations in Set 1 and 2.

the thermal chamber for at least one day to equilibrate prior to the capacity check.

The capacity check consisted of seven constant current charge/discharge cycles at 2–4.2 V (0%–100% SOC based on the manufacturer limits) at 1.5 A, or 0.5 C. A rate of 1 C corresponds to the current that will discharge the nominal capacity of the cell in one hour. Each constant current charge step was followed by a thirty-minute constant voltage step. There was also a 10-minute rest after the CV charge step and the discharge step. During the 7th cycle, the cell was pulse discharged at 1 C for 30 s followed by a 10 s rest to assess the resistance. The mass and discharge capacity distribution for the full lot of cells is shown in Fig. S2. The results of the cells ultimately selected for module cycling are shown in Tables S2–S3.

Module testing protocol.—Following characterization, the cells were placed into the module boards in a discharged state to ensure safety during manual handling. Module cycling was carried out using an Arbin LBT22013 tester. The module board was connected to the main testing channel using 6 AWG wire and ring lung terminations. Auxiliary voltage channels were used to monitor voltages of all eight cells in each board as well as the current through all parallel branches. A K- or T-type thermocouple was attached to the skin of each cell under test with Kapton tape to monitor the cell skin temperature. The modules were placed in Espec SH-662 bench-top type environmental chambers. The chambers were maintained at 25 °C during module cycling.

The module cycling protocol consisted of constant current charge and discharge with 30 min rests in between. Each module completed two hundred cycles at "mild conditions" (2.5–4.1 V cell voltage window and 0.5 C/0.5 C charge/discharge) and two hundred cycles at "aggressive conditions" (2.3–4.2 V cell voltage window and 0.5 C/1.5 C charge/discharge). More aggressive conditions were

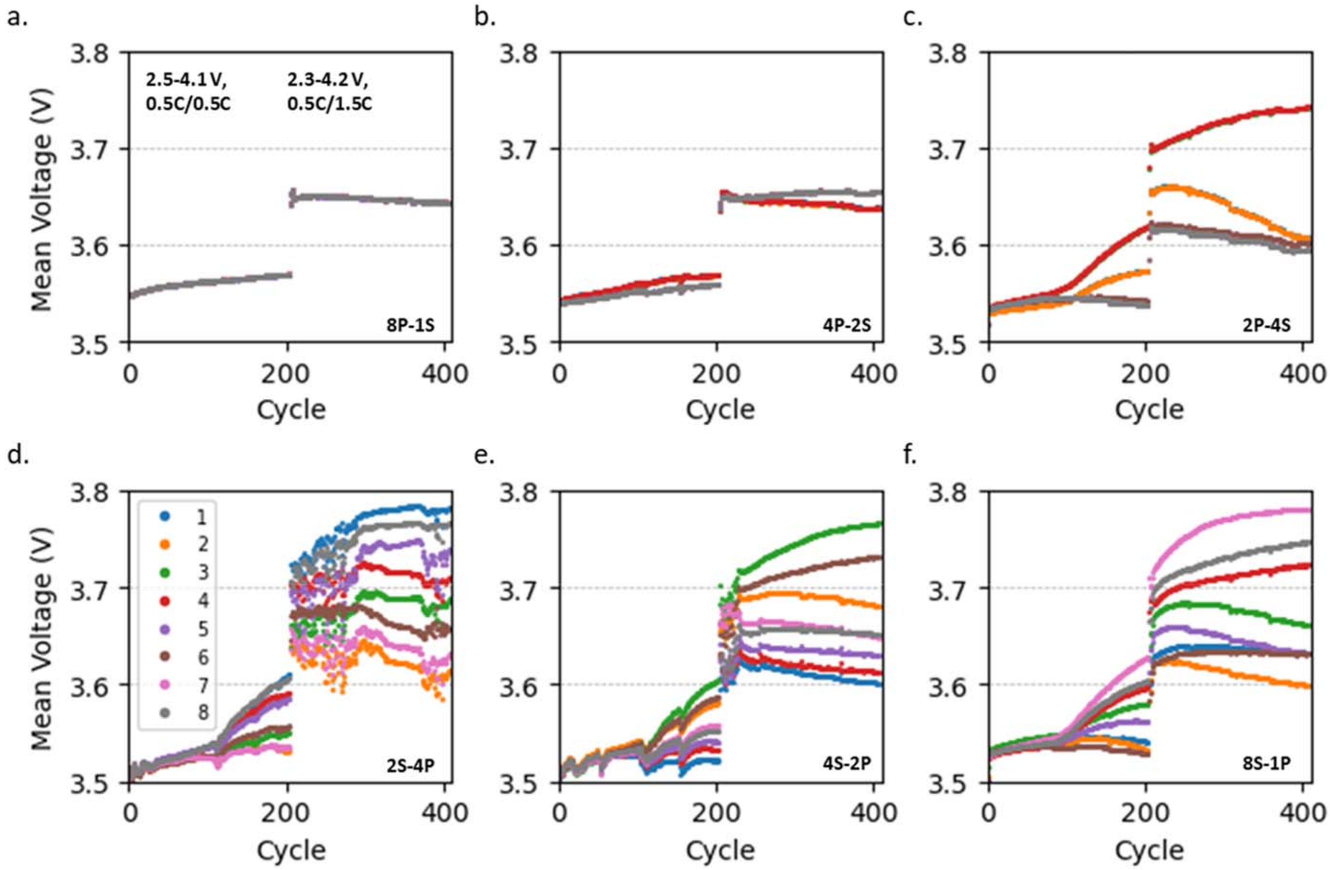

Figure 5. Mean cell voltage per cycle for all modules in Set 1: (a) 8P-1S, (b) 4P-2S, (c) 2P-4S, (d) 2S-4P, (e) 4S-2P, and (f) 8S-1P. Each color indicates the mean voltage per cycle of a specific cell in the module, in positions 1–8 (as indicated in Fig. 2). The individual cell voltages overlap for the parallel subunits in a-c. The first 200 cycles have cell voltage limits of 2.5–4.1 V and charge/discharge rates of 0.5 C/0.5 C. The final 200 cycles have cell voltage limits of 2.3–4.2 V and charge/discharge rates of 0.5 C/1.5 C.

applied to accelerate the emergence of any performance differences between the different module configurations. The current used for each different module configuration is listed in Table S4. Fifty cycles were completed at a time and the data assessed for issues before cycling was restarted.

The module cycling tests did not use a battery management system or passive/active balancing. The objective of the study was to understand the "worst-case" scenario of cycling with no intervention for different module configurations. A charge or discharge step was considered completed once any cell in a module reached the voltage limit (e.g., 4.1 V during charge or 2.5 V at discharge, during the first 200 cycles). Figure S3 shows the implementation of these voltage limits for one cycle of the 8S-1P module. For safety, the cycling program had abort limits based on cell-level voltage, current, and temperature (from manufacturer's specifications) and the module-level voltage and current. None of the cells or modules exhibited any sudden changes in voltage or other measured quantities indicative of major faults.

Results and Discussion

The objective of this study was to investigate the impact of different module configurations on battery performance and degradation. We selected an eight-cell module as a platform because it offered a reasonable number of permutations to study. We examined both parallel-before-series and series-before-parallel configurations: 8P-1S, 4P-2S, 2P-4S, 2S-4P, 4S-2P, and 8S-1P (Fig. 2).

In the automotive and energy storage industries, battery modules typically consist of hundreds or thousands of cells depending on application requirements and cell format.[56] Modules are designed in a parallel-before-series configuration to simplify battery management. Battery management systems typically provide cell-level voltage sensing. The voltage of parallel cells is equal, so the parallel-before-series approach requires a reduced number of sensed voltages in comparison with a series-before-parallel combination of the same number of cells. However, in the series-before-parallel approach, a fault can be isolated using a single fuse for the full string. The post-fault system may continue to operate at a reduced capacity. For this reason, the series-before-parallel approach is favored in applications requiring high reliability or remote deployment, where maintenance and repair operations are impractical.

In a typical module, the data collected includes the voltage of each group of parallel cells and the temperature at one or a few points in the module. Cell-level voltage, current, and temperature measurements are uncommon due to the additional cost and wiring complexity. For this study, we designed a board that enabled minimally-invasive cell-level voltage, current, and temperature monitoring to better understand the cause of different module behaviors.

Energy throughput.—Discharge energy throughput was the first metric used to compare the different module configurations (Fig. 3). In theory, all modules should exhibit the same energy throughput, as they began cycling with cells at similar states of health (see Table S2–S3 in SI). However, for both Set 1 (Fig. 3) and Set 2 (Fig. S6), the discharge energy throughput over the course of 400 cycles was on average 10% higher for the parallel first modules (8P-1S, 4P-2S, and 2P-4S) than for the series-first modules (2S-4P, 4S-2P, and 8S-1P). Note that the discharge energy measurements at the module level were obtained directly from the battery tester.

Figure 4 shows the discharge energy fade rate for the two extreme module configurations, 8P-1S and 8S-1P, with both sets of cells. According to the initial cell characterization (Table S3), the cells in the all-parallel and all-series modules in Set 1 had the same starting average capacity (2.780 Ah vs 2.782 Ah, respectively), standard deviation (0.077 Ah vs 0.068 Ah, respectively), and difference in capacity between the strongest and weakest cell (0.198 Ah vs 0.192 Ah, respectively). However, cell balancing within the parallel module likely led to an overall higher initial energy for the module as well as a lower degradation rate. This cell balancing is discussed further in the current distribution section. The cells in Set 2 show the same behavior.

Voltage spread.—The lower discharge energy throughput in configurations with more cells in series is attributed to cell-level voltage spread. Figure 5 shows the mean cell voltage per cycle (encompassing the charge, discharge, and rest periods) for each cell in each module in Set 1. Comparable results for Set 2 are presented in Fig. S8. Since there was no active or passive cell balancing during cycling, the data reflect the worst-case scenario for module performance. The cell voltage spread results provide a baseline for understanding the degree of intervention required by a battery management system.

As expected, parallel cells balance. The cells in the 8P-1S module (Fig. 5a) maintain the same mean voltage per cycle for the duration of the experiment. Similarly, the cells within each parallel subunit of the 4P-2S module (Fig. 5b) and 2P-4S module (Fig. 5c) also exhibit consistent mean voltages per cycle. However, as cycling progresses, the voltages of the subunits in each module diverge. This spread is more pronounced for the subunits of the 2P-4S module than the 4P-2S module.

By the end of 400 cycles, the mean cell voltages in the series-first configurations (Figs. 5d–5f) spread by nearly 0.2 V. To identify the cause of the spread in mean cell voltage per cycle, we considered the spread of the cell voltage during charge and discharge.

Figure 6a shows the difference of the upper and lower cell voltages at the end of each charge step. Each module ceased charging and transitioned to the rest step once the first cell reached the cut-off voltage of 4.1 V during the first 200 cycles or 4.2 V during the next 200 cycles. As a result, all other cells remained incompletely charged and have lower voltages. Figure 7d illustrates an example where one cell reached 4.1 V (the upper, or cut-off, voltage), triggering the end of charge, while the other cells were incompletely charged, with voltages ranging from approximately 3.95 to 4.05 V. In this case, 3.95 V is considered the lower cell voltage at the end of charge. The difference between the upper and lower cell voltages at the end of charge, as shown in Fig. 6a, shows almost no change over the course of four hundred cycles for all modules.

By contrast, Fig. 6b shows a 0.9 V difference between the lower and upper cell voltages at the end of discharge. Each module stopped discharging and transitioned to the rest step once the first cell reached the cut-off voltage of 2.5 V during the first 200 cycles or 2.3 V during the next 200 cycles. All the other cells would be incompletely discharged and have higher voltages. Figure 7g provides an example where one cell reached 2.5 V (the lower, or cut-off, voltage), triggering the end of discharge, while the other cells were incompletely discharged, with voltages ranging from approximately 2.58 to 2.75 V. In this case, 2.75 V is considered the upper cell voltage at the end of discharge. The difference of the upper and lower cell voltages at the end of discharge, as shown in Fig. 6b, is 0 V for the 8P-1S module and remains relatively constant, about 0.15 V, for the 4P-2S module. The voltage difference of the cells in the 2P-4S module begins at 0.15 V and grows to about 0.65 V after 400 cycles; even in a parallel first configuration, introducing more cells in series leads to notable spread in cell voltages. The cell voltage spread is nearly the same, around 0.9 V, for all the series-first modules. Fig. S9 shows similar outcomes for Set 2.

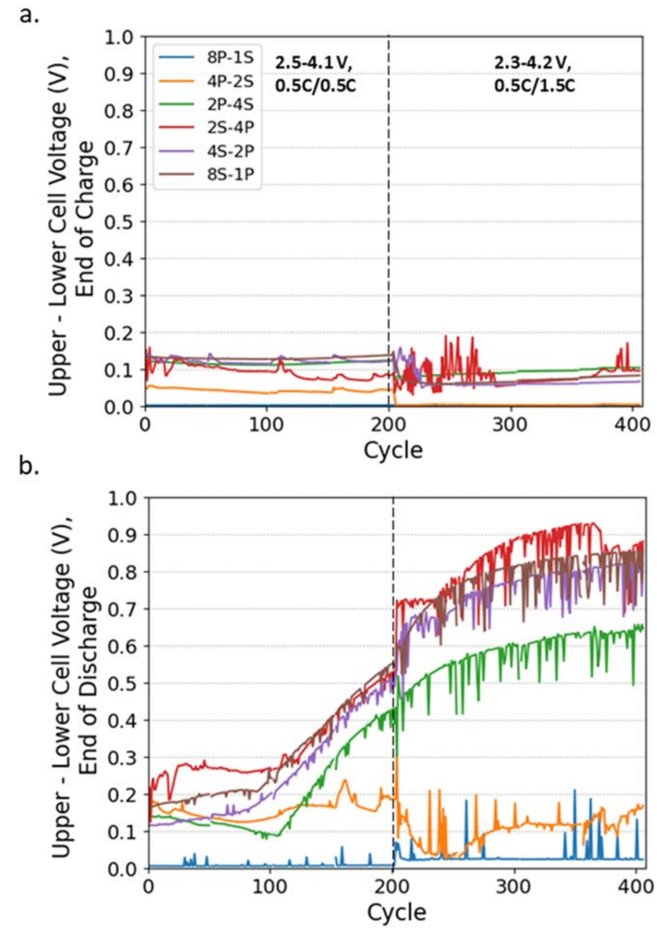

Figure 6. Cell voltage spread in all modules in Set 1 at (a) end of charge and (b) end of discharge. Each color refers to a specific module configuration. The first 200 cycles have cell voltage limits of 2.5–4.1 V and charge/discharge rates of 0.5 C/0.5 C. The final 200 cycles have cell voltage limits of 2.3–4.2 V and charge/discharge rates of 0.5 C/1.5 C.

The greater voltage divergence at the end of discharge is attributed to the differing shapes of the charge and discharge voltage curves. Figure 7 shows the charge and discharge voltage curves of all cells in the 8S-1P module at Cycles 2, 200, and 400. For these NMC cells, the discharge voltage curve exhibits a steep decline after approximately 3.2 V whereas the charge voltage curve follows a steady trajectory to the end of charge. The voltage spread is exacerbated at Cycle 400 due to the higher discharge rate. Fig. S10 shows similar outcomes for Set 2.

Current distribution.—In addition to energy throughput and voltage spread, the modules also differed in the nature of the current flow. Figure 8 shows the current experienced by each branch in all modules in Set 1 during the first five hours of cycling. Figure S11 shows comparable results for Set 2. In parallel-first configurations (8P-1S, 4P-2S, and 2P-4S), the number of distinct branches, or current flows, is equivalent to the number of cells and in series-first configurations (2S-4P, 4S-2P, and 8S-1P), the number of parallel strings. Each module was charged and discharged at 0.5 C; thus, in the ideal case, 1.5 A (0.5 C at the cell-level) should have flowed to each cell. In Fig. 8, all modules exhibit average cell currents of 1.5 A during charge, 0 A at rest, and −1.5 A during discharge. However, there are clearly uneven currents among parallel cells or strings.

Parallel cells or strings of cells (branches) are driven to a common terminal voltage, with current from a source or load distributing among the branches based on their total impedance. Additionally, currents can flow between branches during charge or

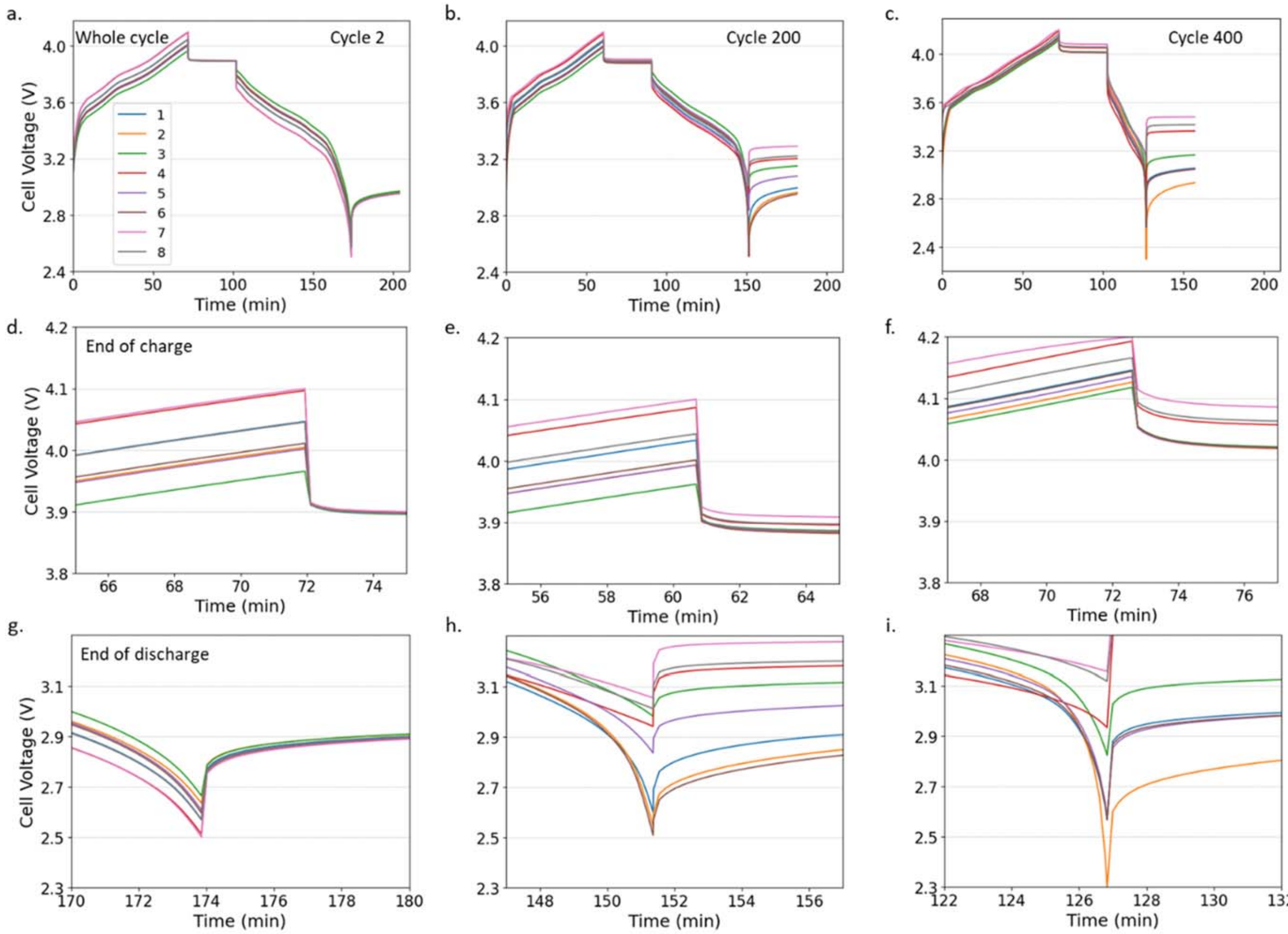

Figure 7. Cell voltages in 8S-1P module in Set 1 during cycle 2 (a, d, and g), cycle 200 (b, e, and h), and cycle 400 (c, f, and i). Each column shows the voltage curves for the whole cycle, a zoom in at the end of charge, and a zoom in at the end of discharge. Each color indicates the voltage of a specific cell in the module, in positions 1–8 (as indicated in Fig. 2). The first 200 cycles have cell voltage limits of 2.5–4.1 V and charge/discharge rates of 0.5 C/0.5 C. The final 200 cycles have cell voltage limits of 2.3–4.2 V and charge/discharge rates of 0.5 C/1.5 C.

discharge, or rest (when no load is applied) to achieve that common voltage. In an ideal battery pack, current would be evenly split among the branches. However, uneven currents in parallel strings can arise due to slight cell-to-cell variations, additional resistances from interconnects, and thermal gradients that affect the resistance of individual branches.[35,57] While the balancing of branches is an accepted phenomenon, there is limited experimental data to quantify the magnitude of the current balancing. Typically, battery packs do not have cell-level current measurements, and battery management systems treat parallel cells as a single unit with uniform current and voltage.

Figure 8 shows that branches can experience currents exceeding 50% from the average. For example, in the 8P-1S configuration (Fig. 8a), the current through Cell 1 during charge peaks at 2 A while Cell 7 experiences a low of 1.2 A. At the beginning of discharge, the current through Cell 1 reaches 2.5 A while the current through Cell 7 is 1 A. Similar deviations from the average current of 1.5 A are observed in the 4P-2S, 2P-4S, and 2S-4P modules. The variation in the current flow is notable given the efforts made to produce modules with branches of equivalent resistance. All the modules in the present study contained cells from the same manufacturer's lot and of comparable state-of-health (see Fig. S1 and Tables S2–S3).

Previous experimental studies have reported similar magnitudes and patterns of current balancing among parallel cells. Notably, Liu et al. used shunt resistors to quantify the current flow through 5 Ah NMC-LCO Li polymer cells in a 6P-1S module during discharge at rates of 0.25 C, 0.5 C, 0.75 C, and 1 C (the module was not cycled).[30] The heterogeneity of the cell currents increased with C-rate. At 0.25 C, the standard deviation reached 0.5 and at 1 C, the standard deviation peaked at 2. In all cases, they observed current "waviness" similar to that in Fig. 8. The study also successfully simulated the current flow through all cells, at C-rates up to 0.5 C, using a single particle model that factored in cell, busbar, and contact resistances. In a later study, Brett et al. used Hall-effect sensors to measure current flow among 2 Ah 18650 NMC/graphite cells in an 8P-1S module.[35] The module was charged and discharged at 1 C a single time (no cycling) in a common-end configuration (terminals at the same end of the module) and an opposite-end configuration (terminals at opposite ends of the module). Although the average current through each cell should have been 2 A at 1 C, some cells experienced currents as high as twice that amount. The authors also emphasized the "complex current response… of plateaus and waves," attributing it to the variation in each cell's internal resistance as it was charged or discharged.

Unlike previous reports, this study monitored current balancing over the course of extensive cycling. Figure 9 shows the current flow in the 8P-1S module in Set 2 at twelve different points over the course of 400 cycles. Cycles 1, 2, 5, 50, 150, and 200 are from the mild cycling protocol and cycles 201, 202, 205, 250, 350, and 400 are from the aggressive protocol. Results for Set 1 are in Fig. S12; Set 2 is presented here as it has the complete current flow for the critical first cycle (complete data for Set 1 begins at Cycle 2). The reduction in current balancing from Cycle 1 to 5 and Cycle 201 to 205, especially during the charge phase, suggests that there is a

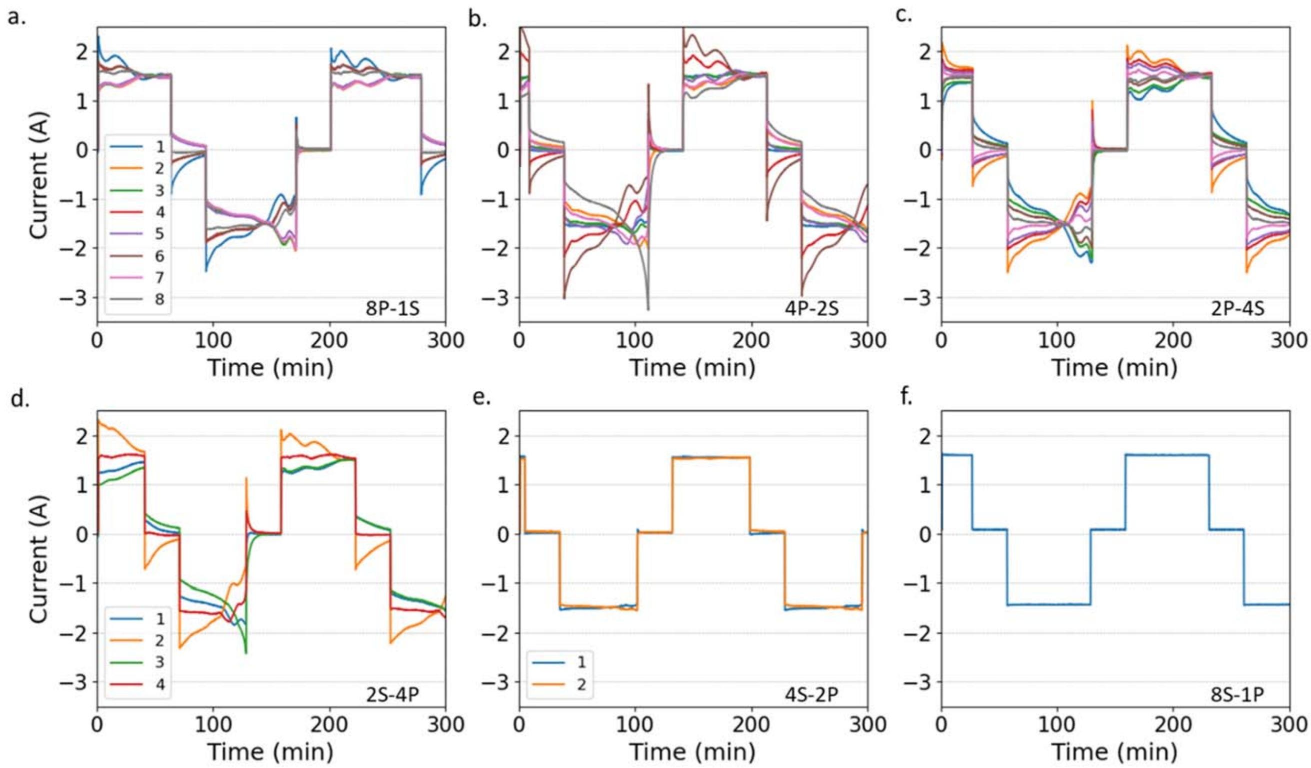

Figure 8. Current balancing among all modules during the first five hours of cycling for Set 1. Each color corresponds to a distinct current flow. In parallel-first modules (a)–(c), the number of current flows is equivalent to the number of cells. In series-first modules (d)–(f), the number of current flows is equivalent to the number of parallel strings.

startup transient. These results highlight the importance of measuring current balancing beyond a single charge or discharge step. Nonetheless, the degree of current balancing in parallel cells over the course of the full cycling experiment is still notable. There is some reduction in the current balancing from Cycle 5 to 200 and Cycle 205 to 400 that is indicative of cell properties converging across the parallel string. A future study will further investigate the impact of parallelization on module performance, including cell energy throughput and degradation, and the role of cell position and temperature heterogeneity.

***Implications for module design and management.*—**The above results offer several key insights into the performance and management of different module configurations. The energy throughput and voltage spread data highlight the value of increasingly parallel configurations in supporting passive cell balancing, at least for NMC cells. The discharge energy throughput was on average 10% higher for the parallel-first modules than the series-first modules because the former did not experience voltage spread. Voltage spread limits the amount of energy that can be extracted from the overall module because each charge or discharge step is limited by the weakest cell.

Some voltage spread is inevitable due to cell-to-cell variation from manufacturing tolerances and thermal imbalances in a system. The issue of manufacturing tolerances will become much more significant as more and more new battery factories come online in the next few years. Normally, voltage imbalances are addressed by passive balancing with shunt resistors or active balancing with converters,[58] but putting more cells in parallel offers an alternative solution.

A consequence of parallel-first configurations is more dramatic current redistribution, both during application of a load and at rest. The instantaneous cell-level current was at times over 50% above the expected value (assuming equal distribution of the module current between all parallel branches) and this has safety implications, especially at higher currents. However, it is important to note that the current redistribution is also impacted by interconnect resistances. Module designs with low interconnect resistances relative to cell resistances, as in this study, may experience higher current redistribution than modules with high interconnect resistances.

Emerging trends in power electronics are encouraging consideration of more parallel configurations. Currently, standard practices for battery module design are driven by minimum voltage requirements from the power electronics interface. This is especially true in grid-connected applications, where the battery interface is a single-stage voltage source inverter. Consequently, the battery voltage must, at all times and all states of aging, exceed the peak line-line AC voltage of the inverter. To produce sufficient voltage for a utility application, many series cell connections are needed. This arrangement is acceptable up to perhaps 1000 V or 1500 V, but its scalability beyond this point is limited. An alternative is to use DC-DC converters to boost battery voltages before connection to the inverter's DC link. There are several benefits to this approach, including improved voltage/power scalability, support for disparate storage technologies within the same installation (i.e. hybridization), and tolerance to individual battery failures without complete system shutdown.[59–62] Additionally, the DC-DC converter frees the battery design from the minimum voltage constraint, enabling battery designers to consider more parallel configurations. The data in this article ultimately enables consideration of module configurations that are best for the batteries rather than the power electronics.

Conclusions

In this work, we quantified the impact of six different NMC-cell module configurations (8P-1S, 4P-2S, 2P-4S, 2S-4P, 4S-2P, and 8S-1P) on overall energy throughput, voltage spread, and current distribution during cycling in the absence of balancing. After 400 cycles, parallel-first configurations such as 8P-1S exhibited over 10% higher energy throughput than series-first configurations. The lower energy throughput of series-first configurations was attributed

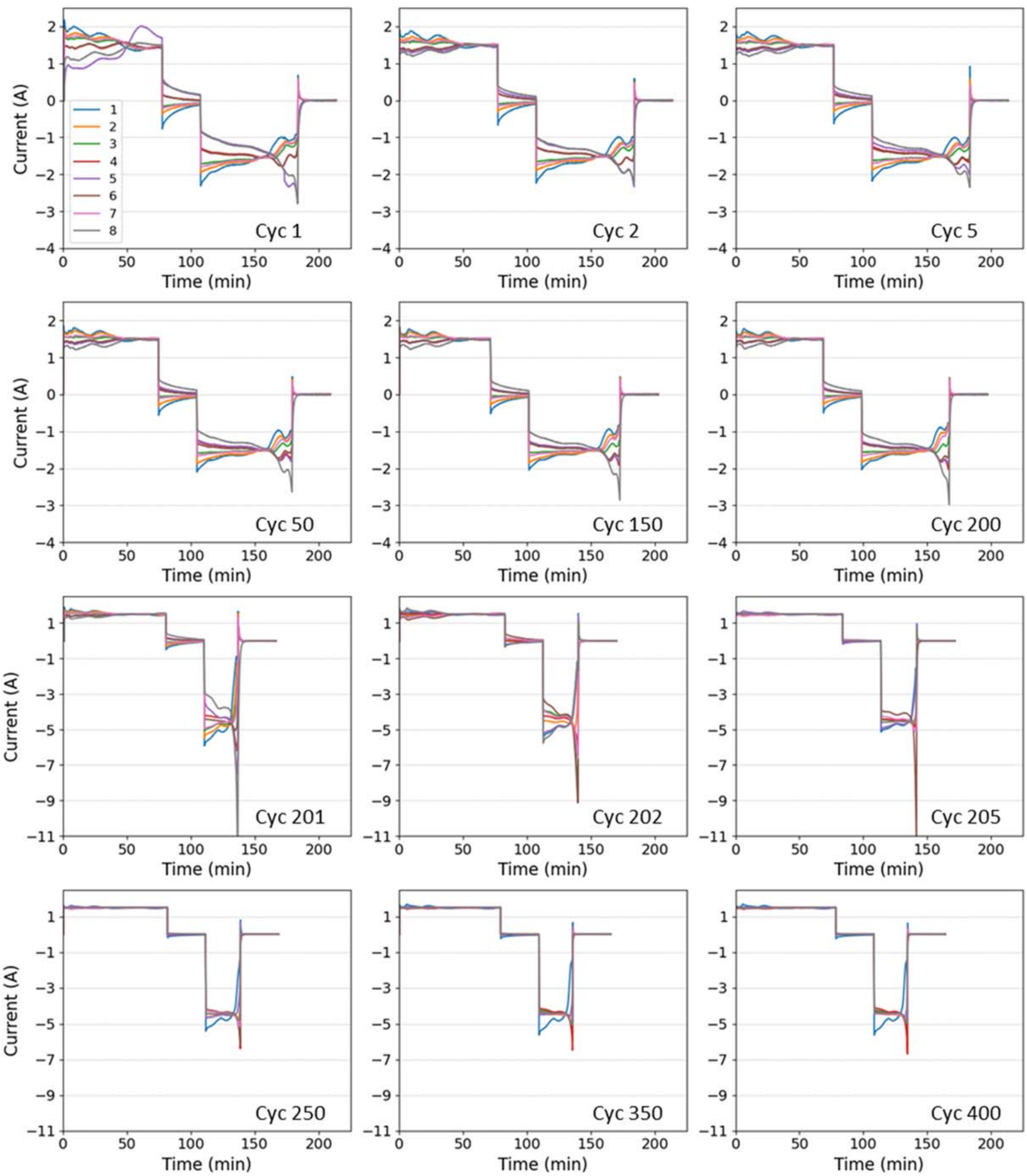

Figure 9. Current balancing in 8P-1S module, Set 2 at Cycle 1, 2, 5, 50, 150, 200, 201, 202, 205, 250, 350, and 400. Each color indicates the current of a specific cell in the module, in positions 1–8 (as indicated in Fig. 2). Cycles 1–200 were completed at more mild conditions: 2.5–4.1 V, 0.5 C/0.5 C charge and discharge. Cycles 201–400 were completed at more aggressive conditions: 2.3–4.2 V, 0.5 C/1.5 C charge and discharge.

to cell-level voltage divergence at the end of discharge, where the voltage curve is steeper. Additionally, parallel-first configurations exhibited notable current rebalancing, with some cells periodically experiencing currents over 30% higher than the average.

This work supports the design of optimal module configurations and control algorithms for different applications, factoring in the "pack penalty" that arises when individual cells are combined into a larger unit. Furthermore, the availability of a broad dataset of module cycling with cell-level monitoring enables the validation and improvement of existing battery pack simulations, which are often developed by scaling single-cell cycling results. The experimental data will be made available on www.batteryarchive.org. Future work will focus on the impact of parallelization on cell level state-of-health, as well as the consequences of different battery management system and power converter architectures.

Acknowledgments

This material is based upon work supported by the U.S. Department of Energy, Office of Electricity (OE), Energy Storage Division. We thank David Rosewater for reviewing this manuscript. This article has been authored by an employee of National Technology & Engineering Solutions of Sandia, LLC under Contract No. DE-NA0003525 with the U.S. Department of Energy (DOE). The employee owns all right, title and interest in and to the article and is solely responsible for its contents. This article has been authored by an employee of Oak Ridge National Laboratory under Contract No. DE-AC05–00OR22725 with UT-Battelle, LLC. The United States Government retains and the publisher, by accepting the article for publication, acknowledges that the United States Government retains a non-exclusive, paid-up, irrevocable, world-wide license to publish or reproduce the published form of this article or allow others to do so, for United States Government purposes. The DOE will provide public access to these results of federally sponsored research in accordance with the DOE Public Access Plan https://www.energy.gov/downloads/doe-public-access-plan.

ORCID

Yuliya Preger https://orcid.org/0000-0001-8558-2529
Srikanth Allu https://orcid.org/0000-0003-2841-4398

References

1. M. Ecker, N. Nieto, S. Käbitz, J. Schmalstieg, H. Blanke, A. Warnecke, and D. U. Sauer, *J. Power Sources*, **248**, 839 (2014).
2. T. Waldmann, M. Wilka, M. Kasper, M. Fleischhammer, and M. Wohlfahrt-Mehrens, *J. Power Sources*, **262**, 129 (2014).
3. Y. Preger, H. M. Barkholtz, A. Fresquez, D. L. Campbell, B. W. Juba, J. Romàn-Kustas, S. R. Ferreira, and B. Chalamala, *J. Electrochem. Soc.*, **167**, 120532 (2020).
4. P. Mohtat, S. Lee, J. B. Siegel, and A. G. Stefanopoulou, *J. Electrochem. Soc.*, **168**, 100520 (2021).
5. T. Li, Z. Zhou, A. Thelen, D. A. Howey, and C. Hu, *Cell Reports Physical Science*, **5**, 101891 (2024).
6. A. J. Crawford, Q. Huang, M. C. W. Kintner-Meyer, J.-G. Zhang, D. M. Reed, V. L. Sprenkle, V. V. Viswanathan, and D. Choi, *J. Power Sources*, **380**, 185 (2018).
7. M. Elliott, L. G. Swan, M. Dubarry, and G. Baure, *Journal of Energy Storage*, **32**, 101873 (2020).
8. N. Kim, N. Shamim, A. Crawford, V. V. Viswanathan, B. M. Sivakumar, Q. Huang, D. Reed, V. Sprenkle, and D. Choi, *J. Power Sources*, **546**, 231949 (2022).
9. B. Ellis, C. White, and L. Swan, *Journal of Energy Storage*, **66**, 107409 (2023).
10. F. Baronti, R. Di Rienzo, N. Papazafiropulos, R. Roncella, and R. Saletti, *IEEE International Electric Vehicle Conference* (2014).
11. D. Sasaki, S. Tsukiyama, M. Matsunaga, J. Miyamoto, and S. Takahashi, *15th International Symposium on Communications and Information Technologies* (2015).
12. H. Zou, H. Zhan, and Z. Zheng, *International Conference on Sensing, Diagnostics, Prognostics, and Control* (2018).
13. K. Rumpf, A. Rheinfeld, M. Schindler, J. Keil, T. Schua, and A. Jossen, *J. Electrochem. Soc.*, **165**, A2587 (2018).
14. I. Zilberman, J. Schmitt, S. Ludwig, M. Naumann, and A. Jossen, *Journal of Energy Storage*, **32**, 101828 (2020).
15. A. Abdellahi, S. Atalay, and A. Rajan, *J. Power Sources*, **508**, 230246 (2021).
16. C. Luan, C. Ma, C. Wang, L. Chang, L. Xiao, Z. Yu, and H. Li, *Journal of Energy Storage*, **41**, 102896 (2021).
17. E. Hosseinzadeh, S. Arias, M. Krishna, D. Worwood, A. Barai, D. Widanalage, and J. Marco, *Appl. Energy*, **282**, 115859 (2021).
18. Y. Tian, Z. Huang, X. Li, and J. Tian, *Energy*, **239**, 122181 (2022).
19. F. Porpora, M. D'Arpino, Y. Cheng, G. Rizzoni, and G. Tomasso, *IEEE Access*, **11**, 96693 (2023).
20. K. Kim and J.-I. Choi, *Appl. Energy*, **352**, 121888 (2023).
21. R. Gogoana, M. B. Pinson, M. Z. Bazant, and S. E. Sarma, *J. Power Sources*, **252**, 8 (2014).
22. X. Gong, R. Xiong, and C. C. Mi, *IEEE Trans. Ind. Appl.*, **51**, 1872 (2015).
23. M. J. Brand, M. H. Hofmann, M. Steinhardt, S. F. Schuster, and A. Jossen, *J. Power Sources*, **334**, 202 (2016).
24. C. Pastor-Fernández, T. Bruen, W. D. Widanage, M. A. Gama-Valdez, and J. Marco, *J. Power Sources*, **329**, 574 (2016).
25. T. Bruen and J. Marco, *J. Power Sources*, **310**, 91 (2016).
26. M. Dubarry, A. Devie, and B. Y. Liaw, *J. Power Sources*, **321**, 36 (2016).
27. A. Fill, S. Koch, A. Pott, and K.-P. Birke, *J. Power Sources*, **407**, 147 (2018).
28. M. H. Hofmann, K. Czyrka, M. J. Brand, M. Steinhardt, A. Noel, F. B. Spingler, and A. Jossen, *Journal of Energy Storage*, **20**, 120 (2018).
29. J. Lv, S. Lin, W. Song, M. Chen, Z. Feng, Y. Li, and Y. Ding, *Appl. Energy*, **252**, 113407 (2019).
30. X. Liu, W. Ai, M. Naylor Marlow, Y. Patel, and B. Wu, *Appl. Energy*, **248**, 489 (2019).
31. A. Fill, S. Koch, and K. P. Birke, *Journal of Energy Storage*, **23**, 37 (2019).
32. M. Schindler, A. Durdel, J. Sturm, P. Jocher, and A. Jossen, *J. Electrochem. Soc.*, **167**, 120542 (2020).
33. A. Fill, T. Schmidt, T. Mader, R. Llorente, A. Avdyli, B. Mulder, and K. P. Birke, *Journal of Energy Storage*, **32**, 101929 (2020).
34. P. Jocher, M. Steinhardt, S. Ludwig, M. Schindler, J. Martin, and A. Jossen, *J. Power Sources*, **503**, 230030 (2021).
35. R. Luca, M. Whiteley, T. Neville, T. Tranter, J. Weaving, J. Marco, P. R. Shearing, and D. J. L. Brett, *Energy Technology*, **9**, 2001014 (2021).
36. W. Shi, X. Hu, J. Wang, J. Jiang, Y. Zhang, and T. Yip, *Electrochim. Acta*, **196**, 13 (2016).
37. N. Yang, X. Zhang, B. Shang, and G. Li, *J. Power Sources*, **306**, 733 (2016).
38. T. R. Tanim, M. G. Shirk, R. L. Bewley, E. J. Dufek, and B. Y. Liaw, *J. Power Sources*, **381**, 56 (2018).
39. X. Feng, C. Xu, X. He, L. Wang, G. Zhang, and M. Ouyang, *J. Clean. Prod.*, **205**, 447 (2018).
40. G. M. Cavalheiro, T. Iriyama, G. J. Nelson, S. Huang, and G. Zhang, *Journal of Electrochemical Energy Conversion and Storage*, **17**, 021101 (2020).
41. I. Zilberman, S. Ludwig, M. Schiller, and A. Jossen, *Journal of Energy Storage*, **28**, 101170 (2020).
42. M. Al-Amin, A. Barai, T. R. Ashwin, and J. Marco, *Energies*, **14**, 4716 (2021).
43. A. Fill and K. P. Birke, *22nd IEEE International Conference on Industrial Technology (ICIT)* 391 (2021).
44. D. Koster, A. Marongiu, D. Chahardahcherik, C. F. Braun, D. Schulte, and E. Figgemeier, *Journal of Energy Storage*, **62**, 106839 (2023).
45. S. Paul, C. Diegelmann, H. Kabza, and W. Tillmetz, *J. Power Sources*, **239**, 642 (2013).
46. Y. Ueeda, K. Taniguchi, G. Kaneko, T. Hirota, W.-H. Yang, Y. Kamiya, Y. Daisho, and S. Inami, *2014 IEEE Vehicle Power and Propulsion Conference (VPPC)* (2014).
47. C. Campestrini, P. Keil, S. F. Schuster, and A. Jossen, *Journal of Energy Storage*, **6**, 142 (2016).
48. R. W. Cook, L. G. Swan, and K. P. Plucknett, *Journal of Energy Storage*, **31**, 101561 (2020).
49. Y. Tao, J. Ye, X. Li, Q. Zhang, A. Pan, Q. Liao, and X. Yang, *Materials Science, Energy Technology and Power Engineering III* (2019).
50. M. Schindler, P. Jocher, A. Durdel, and A. Jossen, *J. Electrochem. Soc.*, **168**, 090524 (2021).
51. D. H. Jung, D. M. Kim, J. Park, S. I. Kim, and T. Kim, *Int. J. Energy Res.*, **45**, 16489 (2021).
52. E. Braco, I. San Martín, A. Berrueta, P. Sanchis, and A. Ursua, *IEEE Trans. Ind. Appl.*, **57**, 4107 (2021).
53. X. Wang, Q. Fang, H. Dai, Q. Chen, and X. Wei, *Energy Technology*, **9**, 210072 (2021).
54. D. Juarez-Robles, S. Azam, J. A. Jeevarajan, and P. P. Mukherjee, *J. Electrochem. Soc.*, **168**, 050535 (2021).
55. R. Wittman et al., *J. Electrochem. Soc.*, **170**, 120538 (2023).
56. C. M. Hoff, *Energy Storage Architecture* (Cambridge University Press, Cambridge) (2022).
57. G. Piombo, S. Fasolato, R. Heymer, M. Hidalgo, M. Faraji Niri, S. Onori, and J. Marco, *Journal of Energy Storage*, **84**, 110783 (2024).
58. A. Ashraf, B. Ali, M. S. A. Alsunjury, H. Goren, H. Kilicoglu, F. Hardan, and P. Tricoli, *Energies*, **17**, 1271 (2024).
59. M. Bragard, N. Soltau, S. Thomas, and R. W. De Doncker, *IEEE Trans. Power Electron.*, **25**, 3049 (2010).
60. S. Vazquez, S. M. Lukic, E. Galvan, L. G. Franquelo, and J. M. Carrasco, *IEEE Trans. Ind. Electron.*, **57**, 3881 (2010).
61. V. Fernão Pires, E. Romero-Cadaval, D. Vinnikov, I. Roasto, and J. F. Martins, *Energy Convers. Manage.*, **86**, 453 (2014).
62. N. Mukherjee and D. Strickland, *IEEE Trans. Ind. Electron.*, **63**, 2340 (2015).